

CO on Supported Cu Nanoclusters: Coverage and Finite Size Contributions to the Formation of Carbide via the Boudouard Process

Jimena A. Olmos-Asar,[§] Enrico Monachino,^{†,△} Carlo Dri,^{†,‡} Angelo Peronio,^{†,‡,⊥} Cristina Africh,[‡] Paolo Lacovig,[○] Giovanni Comelli,^{†,‡} Alfonso Baldereschi,[§] Maria Peressi,^{§,||} and Erik Vesselli^{*,†,‡}

[§]Physics Department, University of Trieste, Strada Costiera 11, I-34151 Trieste, Italy

[†]Physics Department, University of Trieste, via Valerio 2, I-34127 Trieste, Italy

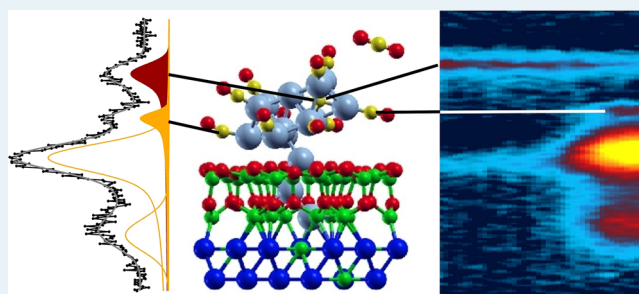
[‡]IOM-CNR Laboratorio TASC, Area Science Park, S.S. 14 km 163.5, I-34149 Basovizza (Trieste), Italy

[○]Elettra-Sincrotrone Trieste S.C.p.A., Area Science Park, S.S. 14 km 163.5, I-34149 Trieste, Italy

^{||}IOM-CNR DEMOCRITOS, I-34136 Trieste, Italy

ABSTRACT: The interaction of carbon monoxide with an ordered array of copper nanoclusters was investigated under ultrahigh vacuum conditions by means of in situ X-ray photoelectron spectroscopy in combination with density functional theory calculations. The Cu clusters were supported on an alumina template grown on the Ni₃Al(111) termination. Adsorption and dissociation of carbon monoxide occur at the copper clusters, yielding accumulation of carbidic carbon at the metal particles through the Boudouard process. The involved mechanisms are investigated at the atomic level, unveiling the effects of cluster finite size, reconstruction, support, and of local CO coverage. It is found that the high coverage of CO at the cluster surface, which considerably exceeds that achievable on single crystal surfaces, facilitates the metal restructuring and the reaction, yielding carbon incorporation into the bulk of the particles.

KEYWORDS: carbon monoxide, copper, clusters, alumina, carbide



1. INTRODUCTION

The interaction of carbon monoxide with copper is a widely investigated topic due to its role in many technologically relevant synthesis processes. An important example is the water gas shift reaction (WGS),^{1,2} where CO and H₂O react to produce hydrogen. The WGS process, as well as its reverse, are involved in several catalytic technologies like methanol synthesis,^{3–6} methanol steam reforming, ammonia synthesis, coal gasification, and many others.¹ One of the elementary subprocesses is the Boudouard reaction, which converts carbon monoxide into carbon dioxide and atomic carbon (2CO → CO₂ + C). Carbon obtained from the Boudouard process can then either take part to the reaction or contribute to the formation of carbidic or even graphenic and graphitic poisoning phases, depending on the catalyst and reaction conditions.⁷ Both in model and applicative contexts, the reaction steps yielding carbon accumulation have a crucial impact in the definition of the actual catalyst's behavior in different contexts, i.e. high pressure reactors,⁸ fuel cells,⁹ liquid electrocatalytic environments,¹⁰ and pure model systems.^{11,12} In the framework of surface science, CO interaction with low-index single crystal surfaces has been studied since the early stages of ultrahigh vacuum (UHV) investigations and subsequently also at higher

pressures.¹³ For long, indeed, the CO–metal systems have been considered as a benchmark for atomic-level investigations by means of many structural and reactivity techniques. More recently, along the way toward the transferability of surface science results to more realistic systems, CO interaction with catalytic surfaces has been elected as a main topic where the progressive development of microscopy and spectroscopy techniques working at higher pressure was exploited.^{14–17} In parallel, in the attempt of bridging the material gap, novel model systems acting as templates for active metal cluster deposition were introduced to mimic applicative dispersed catalysts.^{18–21}

Concerning CO chemistry on catalytic surfaces, it is well-known that the direct dissociation process is strongly endothermic and very unfavorable, with C–O bond energies and breaking barriers typically much higher than the CO binding energy to the surface. Many studies were devoted to investigate the role of surface coordination, e.g. in the case of steps,^{22,23} and of finite size in both free^{24–26} and supported

Received: September 9, 2014

Revised: March 16, 2015

Published: March 18, 2015

cluster systems.^{27–30} Only very recently, it has been observed on ruthenium and platinum that there is an interplay between low surface coordination and CO coverage, both affecting the CO dissociation process.^{29,30} In particular, a Pt surface undergoes extensive and reversible restructuring when exposed to carbon monoxide at near-ambient pressures,³⁰ observing the creation of low-coordination edge reaction sites in the formed nanoclusters. CO coverage that can reach the supra-monolayer limit in clusters affects adsorption energies, heats of reaction, and activation energies on Ru clusters.²⁹ Thus, to understand catalytic processes at the atomic level, it is crucial to explore the structural and chemical evolution of catalysts in situ and in operando and to account for the effects of curved and crowded nanostructured surfaces.^{29,30}

We chose copper clusters supported on an alumina template grown on the Ni₃Al(111) termination as a model system to further investigate this fundamental topic. Copper/alumina catalysts (modified with Pd) have recently been investigated for the selective acetylene hydrogenation process showing interesting behavior.³¹ Alumina supports, obtained by high-temperature oxidation of single crystal terminations of Ni–Al alloys,^{32,33} have already been largely characterized.^{32–41} An ultrathin nonstoichiometric alumina film was shown to be an optimal template for the growth of metallic nanoclusters.^{32,39,42–44} The peculiar structure of Al₂O₃/Ni₃Al(111) is described by a ($\sqrt{67} \times \sqrt{67}$)R12.2° unit cell with a side of 4.15 nm, resulting in the so-called *network* and *dot* structures.³² The latter is characterized by one hole site per unit cell where hot metal atoms impinging from a chemical vapor phase and diffusing at the alumina surface can stick and generate metallic seeds. These seeds act as preferred anchoring sites for the subsequent nucleation and growth of clusters, which are therefore hooked and stabilized by the ordered template, thereby preventing sintering. Although this is not a general rule, since for example Ag and Rh do not grow at these sites,^{40,45} selective or preferential nucleation following the dot structure was observed for many metals like Pd,^{32,46,47} V,^{40,42} Fe,^{43,47} Co,⁴⁷ and, precisely, Cu.^{40,42} In order to investigate the CO reaction mechanism on copper clusters, we therefore chose the ultrathin alumina film grown on Ni₃Al(111) as an optimal template for ordered and stable anchoring of the reactive metallic particles. Unexpected results were obtained, indicating that CO dissociation is a complex process driven by several factors including local coverage, support, finite size effects, and cluster reconstruction.

2. METHODS

2.1. Experimental Section. The Ni₃Al(111) single crystal was treated under UHV by standard sputtering and annealing recipes in order to clean the surface and recover both order and stoichiometry, yielding a sharp (2 × 2) low energy electron diffraction (LEED) diffraction pattern. The alumina ultrathin film was grown by thermal oxidation of the sample at 1000 K in 10^{−7} mbar O₂, following well-known procedures from the literature.^{32,35} The quality of the alumina film was checked both by LEED³⁷ and by comparing the O 1s and Al 2p core level spectra to literature data.³⁵ Core-level X-ray photoelectron spectroscopy (XPS) experiments were performed at the SuperESCA beamline of Elettra, the third generation synchrotron radiation source in Trieste (Italy).⁴⁸ In particular, C 1s spectra were measured at normal emission using 400 eV photons. A Phoibos (SPECS GmbH) hemispherical electron energy analyzer equipped with an in-house developed detector

was used to collect the spectra. A time resolution of about 30 s and a heating rate of 0.15 K/s were chosen for the time-resolved temperature-programmed experiments. After normalization and subtraction of a Shirley background,^{49,50} core level spectra were analyzed by least-squares fitting methods using a Doniach–Sunjic function,⁵¹ convoluted with a Gaussian envelope in order to account for experimental resolution, inhomogeneity, and temperature-induced broadening. Binding energies were calibrated with respect to the Fermi level. Cu atoms were deposited on the sample at room temperature from a chemical vapor phase, obtained by sublimation from a pure Cu rod in a resistively heated tungsten crucible. The actual Cu sample coverage was obtained by correlating the evaporation flux (measured by means of a quartz balance), the Cu 2p_{3/2} XPS signal, and the decay of the Al 2p_{3/2} and O 1s signals as a function of the exposure.

2.2. Theoretical. Theoretical calculations were performed within the density functional theory (DFT) approach implemented in the Quantum-Espresso package,⁵² with ultrasoft pseudopotentials.⁵³ For exchange and correlation the spin unrestricted generalized gradient approximation in the Perdew–Burke–Ernzerhof implementation was used.⁵⁴ Periodic boundary conditions and a slab geometry were applied for the description of the systems with supported clusters. For the selection of the plane waves, energy cutoffs of 35 and 280 Ry to describe the wave function and the electronic density, respectively, were shown to ensure convergence of the results. Considering two layers of Ni₃Al(111) under the oxide, the whole cell contains 1257 atoms already for the substrate (268 atoms in each layer of the alloy and four oxide layers consisting of 132 Al, 188 O, 188 Al, and 213 O, respectively). The Cu clusters and the CO molecules have then to be added, yielding an extraordinarily large cell at the very limit of the computational capabilities. Due to this reason, most of the calculations have been performed using a reduced model containing only a portion of the Al₂O₃/Ni₃Al(111) unit cell around the dot site, plus a Cu₁₃ cluster (with two additional atoms constituting the anchoring seed) and vacuum in all three spatial directions, for a total of about 150 atoms. To check the validity of this model, a test was performed also using a larger cell size for the support (330-atom model), and no meaningful variations were found. The supported Cu₁₃₊₂ cluster has been chosen as an upper limit to the size of the system to comply with the computational limits and because the corresponding free-standing Cu₁₃ cluster is the most stable structure in vacuum, compared to clusters of similar size. However, the presence of the support affects the shape of the cluster, and all the structures used in the calculations have been fully optimized.⁵⁵ The sampling of the first Brillouin zone was performed using a (3 × 3 × 1) *k*-point grid for the calculations of the Cu(111) surface, and the Γ point was used in the cases of free-standing clusters. Despite the reduced models, evaluation of the reaction barriers and paths was not affordable.

3. RESULTS AND DISCUSSION

The evolution of the C 1s core level signal on the alumina template decorated with Cu clusters was followed in situ and in real time during a CO uptake from the gas phase at liquid nitrogen (LN₂) temperature and upon subsequent annealing of the sample in a constant CO background ($p_{\text{CO}} = 5 \times 10^{-9}$ mbar). The results obtained for Cu coverage values (with respect to the clean Ni₃Al surface) of 0.11, 0.36, and 0.68 monolayer (ML, one Cu atom per surface alloy atom) are

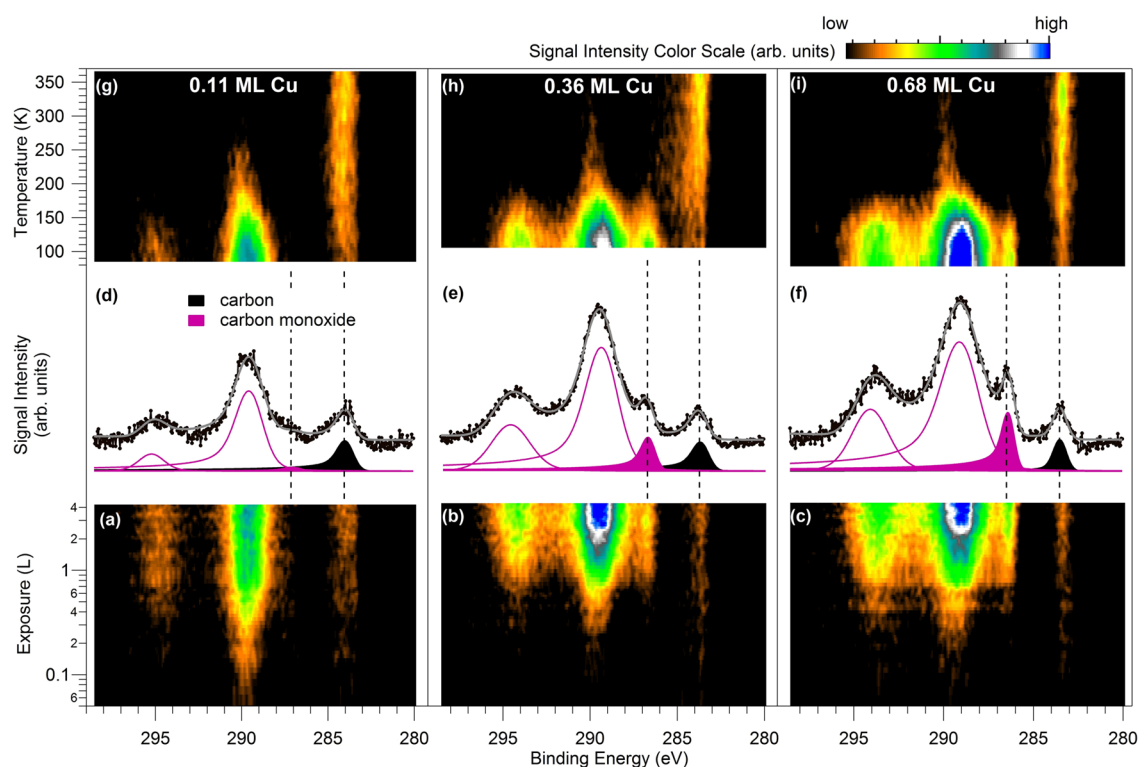


Figure 1. C 1s core level spectra measured in situ upon exposure to CO of alumina-supported Cu for different cluster sizes corresponding to 0.11 (panels a, d, g), 0.36 (panels b, e, h), and 0.68 ML (panels c, f, i) of Cu, respectively. Signal intensities are mapped into a color scale and are reported as a function of CO exposure at LN₂ temperature (bottom panels a–c) and of annealing temperature (upper panels g–i). Core level spectra at saturation at LN₂ temperature are depicted in panels d–f together with the peak deconvolution for atomic carbon (black) and carbon monoxide (magenta). Annealing was performed in a constant CO background of 5×10^{-9} mbar ($h\nu = 400$ eV).

reported in Figure 1. Since it is known that Cu clusters nucleate, anchor, and grow at the hole sites of the alumina dot structure,^{40,42} the average Cu cluster size can be easily calculated as follows. The unit cell side of the Ni₃Al(111) surface is 2.45 Å,^{39,56} yielding a coverage of 3.5×10^{-3} ML of nucleation (hole) sites of the dot structure. Therefore, assuming that all nucleation centers are occupied, 0.11, 0.36, and 0.68 ML of Cu correspond to average cluster sizes of about 30, 100, and 200 atoms, respectively. In the bottom panels (a–c) of Figure 1, the XPS signal intensity in the C 1s region is reported in color scale as a function of CO exposure at LN₂ temperature. In the central panels (d–f), the C 1s spectra of the surface at saturation are shown, together with the best fit and the peak deconvolution. The peaks (black) at 283.5–283.9 eV (depending on the Cu cluster size) are attributed to atomic carbon species (carbide), while the peaks at 286.3–286.9 eV (filled magenta) are due to molecular carbon monoxide adsorbed at the Cu clusters.⁵⁷ Also the remaining peaks (magenta lines) are related to the same carbon monoxide species and originate from inelastic photoemission processes. Indeed, it is well-known that when a core electron is extracted from the CO molecule adsorbed at Cu, a previously unoccupied valence orbital in the molecule is pulled down below the Fermi energy by the attractive core–hole potential.^{58–60} The different time-scale of the photoionization and relaxation phenomena make the wave function of the remaining electrons not an eigenstate of the final-state Hamiltonian, and the filling of this level increases the relaxation energy, thus giving origin to distinct satellites intensities. CO/Cu is a peculiar system from this point of view, and it has therefore been largely investigated in the literature. Both the shape and energy shift of the losses

that we observe in our spectra are in agreement with previous data.^{58–60} As it can be observed in Figure 1, however, for small cluster sizes (panel d), the elastic peak is almost not contributing to the spectrum, whereas the inelastic satellites predominate. This effect modulates with cluster size (from left to right). Switching back to the CO interaction with the clusters, it can readily be noticed that during the uptake at LN₂ temperature (bottom panels of Figure 1) the molecule undergoes dissociation and that atomic carbon accumulates at the clusters. When no further evolution of the C 1s intensities is observed, saturation or equilibrium with the CO background pressure (5×10^{-9} mbar) are actually achieved. Upon heating (in constant CO background pressure), the CO residence time diminishes and desorption is observed, while in parallel the intensity related to the atomic C species increases up to a plateau, which is reached when the CO coverage drops (250–300 K). It therefore appears that CO dissociation may be influenced by the local CO coverage. Both processes, i.e. adsorption and dissociation, are influenced by the sample temperature, by the gas pressure, and likely by the progressive carbon accumulation at the clusters. The latter phenomenon may indeed lead to a progressive deactivation of the cluster due to carburization effects. To further investigate this point, we collected the C 1s core level spectra after saturating the Cu clusters with CO at LN₂ temperature (Figure 2) in equilibrium with the CO background pressure (panel a). We then switched off the gas flux and collected the spectrum again after about 3 min (panel b). What is observed is that in the latter case the CO density at the cluster surface is lower due to spontaneous (or photon induced) desorption, while the C coverage remains unaltered (see the difference spectrum in blue), thus excluding

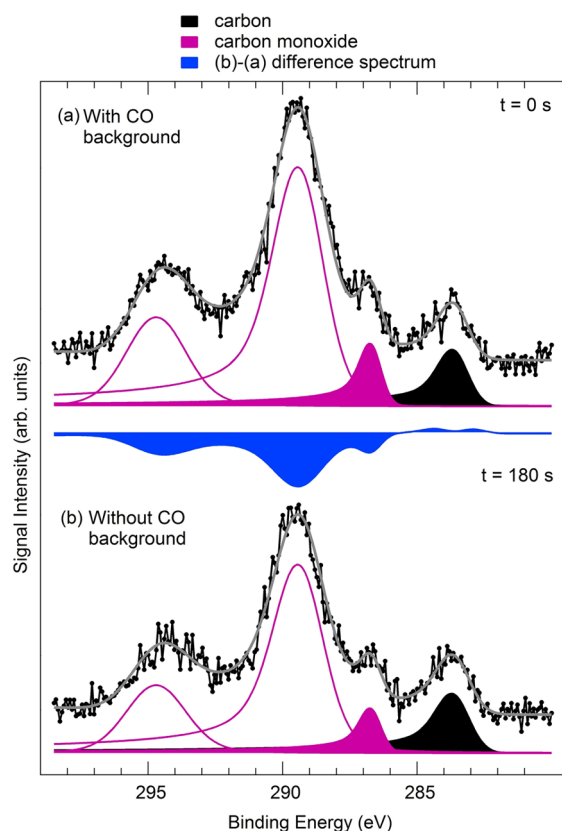


Figure 2. C 1s core level spectra ($h\nu = 400$ eV) from Cu clusters (0.36 ML) supported on alumina, saturated with CO at LN₂ temperature and measured with (panel a) and without (panel b) CO background (5×10^{-9} mbar). Deconvolution of the C (filled black) and CO (filled magenta) adiabatic signals, and of the CO losses (magenta lines), are shown. The blue curve represents the b – a difference spectrum.

at least on this time-scale a contribution from photon-induced CO dissociation. Interestingly, Cu 2p core level spectra (not shown) collected after copper deposition and at the end of the reaction show no significant differences and no relative core level shift, indicating both stability of the clusters up to 370 K and no Cu oxidation. Concerning the role of the cluster size, in Figure 3 we report the C/CO coverage ratios estimated from the corresponding XPS peak areas at two temperatures (LN₂ and room temperature) as a function of the number of atoms in the clusters. A clear size dependence can be observed, showing that the smaller the cluster, the more reactive it is with respect to CO dissociation.

In order to thoroughly understand the mechanisms involved in the observed phenomena, we performed an extensive set of DFT calculations with the aim of elucidating the different factors affecting the reaction. With concern to the Boudouard reaction in the gas phase ($2\text{CO} \rightarrow \text{CO}_2 + \text{C}$) we naturally obtain that it is highly endothermic (+5.32 eV). Regarding the catalyst, the main DFT results are illustrated in Figures 4 and 5. We focused on the role of the clusters finite size, of the support, and of the local surface coverage with respect to candidate reaction mechanisms. We analyzed the energy differences for initial, final, and intermediate states of feasible processes occurring in different Cu-based substrates. Energies and optimized stick-and-ball models are reported in Figure 4. In particular, we considered as a possible initial state the Cu model catalyst with both adsorbed and gas phase CO (blue energy

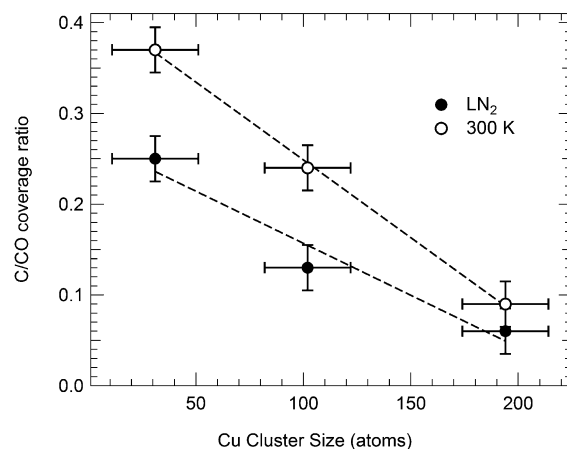


Figure 3. Carbide coverage with respect to CO saturation coverage after exposure of the Cu clusters to CO at LN₂ temperature (filled markers) and at room temperature upon annealing (empty circles) in a CO background (5×10^{-9} mbar).

levels in all panels of Figure 4). Further CO adsorption would lead to the intermediate state for Langmuir–Hinshelwood (LH) mechanisms (orange levels). The decomposition of CO adsorbed on the surface into C(ads) + O(ads) (gray levels) could be both the final state of the direct decomposition or an intermediate state for the whole Boudouard reaction (black levels), yielding C(ads) and CO₂(gas). In all cases energies are referred to the corresponding initial configuration. In panel a, it is shown that on a flat Cu(111) single crystal surface at low coverage direct C–O dissociation is unlikely to occur. If no Cu mobility or only surface reconstruction are allowed, in analogy to previous calculations,^{61,62} high energy states are obtained (3.09 and 2.57 eV, respectively—not shown). However, when allowing for C incorporation into subsurface sites, the energy cost lowers to 2.05 eV (panel a). Further CO adsorption is instead favorable (−0.77 eV). The full Boudouard reaction yields a strongly less stable system by as much as 0.48 eV and is therefore highly unfavorable on the Cu(111) surface. This is in agreement with experimental findings, where low temperature adsorption of CO yields a maximum saturation coverage of 0.5 ML (0.33 ML for the $(\sqrt{3} \times \sqrt{3})\text{R}30^\circ$ structure),⁶³ and dissociation is not observed unless alkali metals are coadsorbed on the surface.⁶⁴ Going to the free-standing cluster system (panel b, Cu₁₃), thus introducing finite-size contributions, in the small coverage limit the energy cost for direct CO(ads) dissociation is already almost half than in the former case. However, the Boudouard reaction is almost equally endothermic (+0.43 eV). Concerning the spin, with one CO molecule attached the system is in a high spin state, while upon adsorption of the second CO molecule the system adopts a low spin state. In order to consider the presence of the support, we then anchor the Cu₁₃ cluster to a Cu₂ seed (Cu₁₃₊₂) fixed in the hole defining the dot structure of the ultrathin alumina layer (panel c). These are precisely the cluster anchoring seeds proposed in the literature for several metals on this alumina template.^{32,40,42} Upon adsorption of a CO molecule in the zero coverage limit on the latter system, again the energy loss for the Boudouard reaction is still high (+0.63 eV). Therefore, neither the finite size, nor the presence of a support seem to favor the C–O breaking process, since both the Boudouard reaction and, even more, the direct CO dissociation, remain highly endothermic.

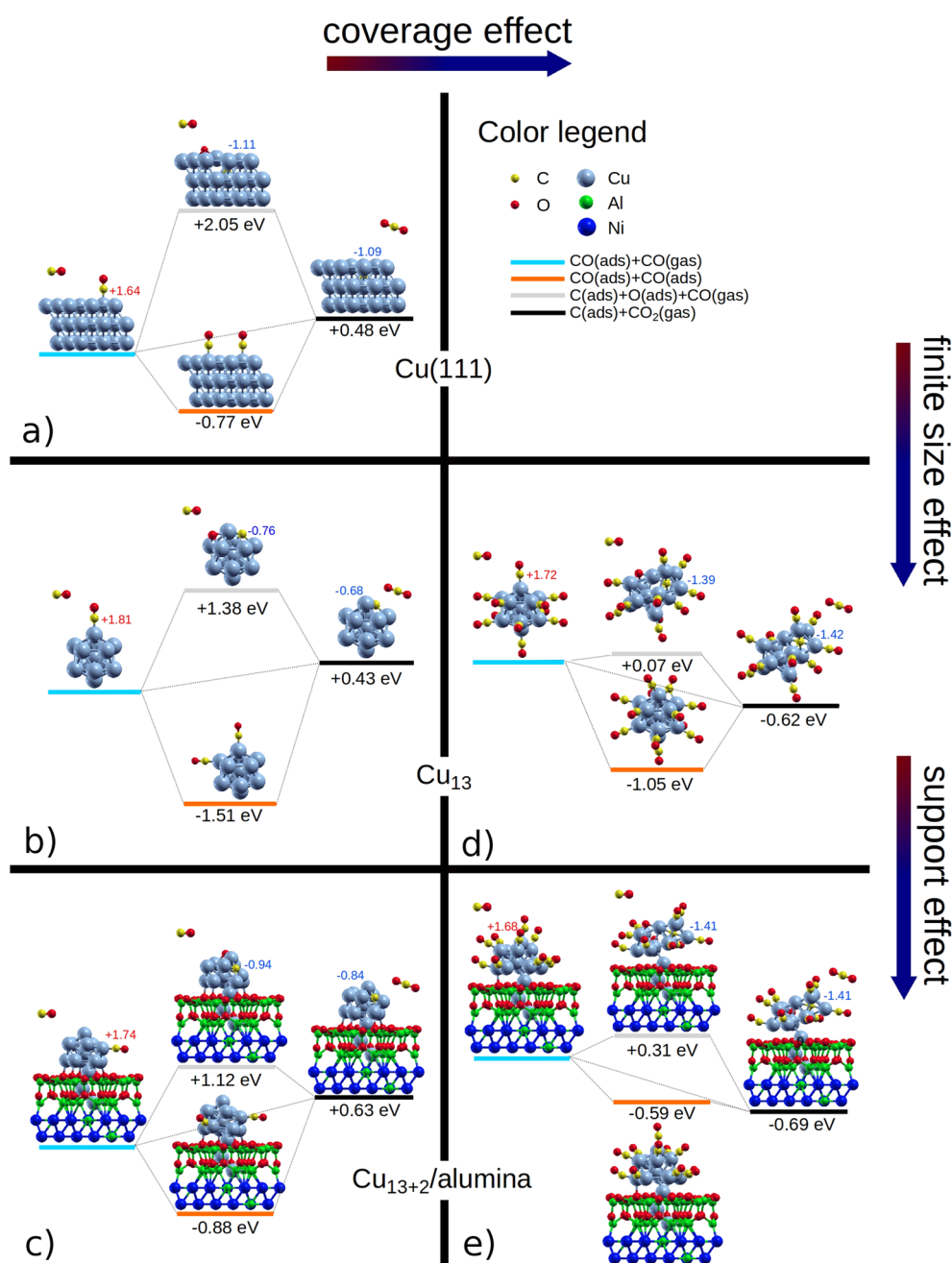


Figure 4. DFT energy diagram for CO reaction pathways on Cu(111) (panel a), unsupported Cu₁₃ cluster (panels b and d), and Cu₁₃₊₂ (with a 2-atom seed) cluster supported on an ultrathin alumina film grown on Ni₃Al(111) (panels c and e). The diagram puts in evidence the role of finite size, support, and coverage effects on the direct CO dissociation, disproportionation, and on the complete Boudouard reaction through ER and LH mechanisms. Bader charges in units of |e| for C atoms are reported (blue negative, red positive).

The experimental results strongly suggest that coverage effects play an important role here. Indeed, when adding also this contribution in the calculations, the picture changes remarkably. On a free-standing Cu cluster with a CO coverage of 1 monolayer (ML, one molecule per surface Cu atom, panel d), there is almost no cost in energy to directly dissociate one of the adsorbed molecules yielding C(ads) and O(ads) atoms (+0.07 eV), while when considering the full Boudouard-like process yielding C(ads) and CO₂(gas), an energy gain is actually obtained (−0.62 eV). On a supported Cu cluster with the same initial CO coverage of 1 ML (panel e), the energy gain for the full Boudouard reaction has a similar value (−0.69 eV), with a final state that is more stable than the coadsorbed

configuration (orange level), characterized by an energy gain of only −0.59 eV with respect to the initial state (blue level). It is important to mention that the higher the CO coverage, the smaller the energy gain upon further CO adsorption, up to saturation, when sticking of an additional molecule from the gas phase is no longer favored: DFT gives −1.05 eV (−1.51 eV) for the 12th (2nd) CO molecule added to a free-standing Cu₁₃ cluster, and −0.59 eV (−0.88 eV) when the cluster is supported. However, as discussed also in the literature,²⁹ on nanosized systems it is easy to reach and overcome the ML coverage, going well beyond the saturation value typical of single-crystal surfaces. In the case of small clusters as the one presented here, increasing the coverage may also lead to

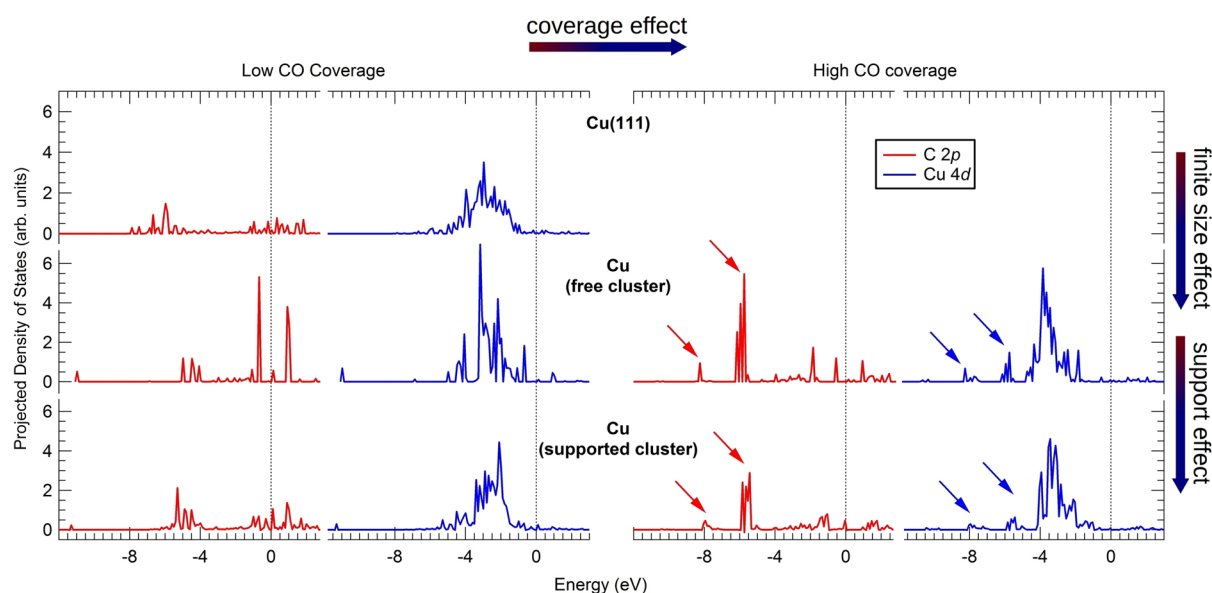


Figure 5. DFT projected density of states on the carbon atom after CO dissociation (red) and on the surrounding Cu atoms (average, blue) as a function of CO coverage (left/right) for the Cu(111) surface, the free-standing Cu cluster, and the supported Cu cluster (from top to bottom).

distortion and restructuring of the cluster. The saturation coverage is different for free-standing and supported clusters; nevertheless for direct comparison we have chosen the same coverage of 1 ML for both cases and in configurations where important distortions are not produced. It can be observed that at high CO coverage the CO–Cu interaction weakens the Cu–Cu bonds making the cluster more malleable and favoring restructuring after CO breaking, yielding incorporation of the carbon atom originating from CO dissociation (panels d and e), at variance with the low-coverage limit where carbon remains at the surface (panels a–c). Since direct C–O breaking is energetically costly, two-molecule disproportionation processes involving Eley–Rideal (ER) or LH mechanisms with formation of CO₂ are likely to occur. Moreover, by means of Bader charge analysis (red and blue numbers in Figure 4, in units of |e|), we can see that favorable final configurations for the C atom after C–O dissociation yield negative values, thus confirming the formation of a carbide state. In Figure 5 we plot the DFT density of states projected on the C atom stemming from CO dissociation and on the surrounding Cu neighbors. While no relevant effects can be observed for size and support contributions (top to bottom), the CO coverage is instead found to significantly change the density of states (left to right). The strong hybridization (arrows) between the C 2p and the Cu 4d states at -5.5 and -8.0 eV could explain the energy gain of carbidic C at high CO coverage, thus favoring CO decomposition in parallel with other coverage-induced effects like cluster distortion and relaxation.

On the basis of the results obtained by means of the calculations performed in the DFT framework, we can therefore explain the observed phenomenon, where CO dissociation occurs already at LN₂ temperature, even if a higher conversion is observed for increasing temperature. Indeed, when considering all the contributing effects of the catalyst's size, of the support, and specifically the effect of coverage, the Boudouard reaction becomes exothermic. Still, kinetic limitations may play a role in practice, since the reaction barriers were not calculated, mainly due to the large number of relevant degrees of freedom. The experimental evidence

suggests small activation energies of the order of few tenths of eV. The size effects of the cluster translate into the higher saturation coverage for CO (1 ML or even larger, as shown in Figure 4, panels d and e) with respect to the single crystal termination (0.5 ML).⁶³ In this sense, finite size effects contribute indirectly to the reaction since the high density of the ad-layer favors CO dissociation. We observe that both the increase of the CO coverage (Figure 4, compare panels b and d) and the interaction with the oxide surface (from panels b to c and d to e) yield restructuring of the metal cluster, with changes in its shape. Size effects can be more complex than what described here, as for example reported for bimetallic nanoparticles, where the variation in activity with particle size is also shape-dependent.⁶⁵ Breaking of CO and distortion of the cluster crystalline structure occur when the CO–Cu interactions become competitive with the Cu–Cu bond energy, making carbon inclusion into the bulk of the copper cluster energetically favorable. It is indeed widely recognized that defective adsorption sites (steps, kinks, low-coordinated defects) show peculiar catalytic activity.³⁰ In addition, thanks to the contribution of the support (Figure 4, panel e) the final state, i.e. the carbidic phase, becomes the lowest in energy with respect to both initial and intermediate states, thus making the Boudouard reaction an exothermic process. Concerning the Cu–O interaction, in the case of low CO coverage we investigated the adsorption and dissociation of CO in different sites of the supported Cu₁₃₊₂ nanocluster (including interfacial sites), finding that the energies of the different initial and final configurations can vary up to 0.6 eV. Changes also in the kinetic barriers of the dissociation process cannot be excluded, as reported in the literature, but we could not tackle this point due to the large size of the system.^{66,67} However, we recall that the cluster does not wet the surface,⁵⁵ and that CO does not stick onto the oxide surface.

4. CONCLUSIONS

By comparing experimental evidence with results obtained within the DFT framework, we have shown that the Boudouard reaction is taking place efficiently at small copper clusters

supported on an ordered ultrathin film alumina template. Remarkably, it is found that the reaction occurs already at LN₂ temperature, indicating a low activation barrier (of a few tenths of an electronvolt), and that the reaction is made possible by the combined contribution of support, finite size effects, cluster reconstruction, and local coverage. The latter is the leading factor for driving the Boudouard reaction, but in turn it is allowed only by the finite size of the clusters. The presence of the support does not change the scenario, but it is essential for making the clusters more malleable and favors the Boudouard process with respect to further adsorption of CO. Among many intermediate configurations related to different reaction steps, direct C–O dissociation is always energy demanding, thus suggesting that disproportionation processes involving ER or LH mechanisms may significantly contribute. Our findings are obviously not directly transferable to systems under applicative working conditions since the pressure gap is significant. In this respect, when leaving the model environment adopted in this study, the temperature–pressure dependent phase diagram of the CO coverage at the clusters should be considered, together with the temperature-driven cluster restructuring and stability. Nevertheless, a thorough insight into this strategically important reaction was obtained at the single-atom level, thus providing useful information for further investigation of more realistic systems.

AUTHOR INFORMATION

Corresponding Author

*E-mail: vesselli@iom.cnr.it

Present Addresses

[△]E.M.: Zernike Institute for Advanced Materials, University of Groningen, Nijenborg 4, 9747AG Groningen, The Netherlands.

[†]A.P.: Institute of Experimental and Applied Physics, University of Regensburg, Universitätsstraße 31, 93053 Regensburg, Germany

Notes

The authors declare no competing financial interest.

ACKNOWLEDGMENTS

We would like to thank M. Schmid for providing the coordinates of the substrate model. E.V., M.P., and A.B. acknowledge financial support from MIUR through Futuro in Ricerca FIRB 2010 project no. RBFR10J4H7. Fondazione Kathleen Foreman Casali, Beneficentia Stiftung, Università degli Studi di Trieste through project FRA 2012, and Italian Ministry of Foreign Affairs, Directorate General for the Country Promotion through the Executive Program with Argentina, are also acknowledged for their contribution. J.O.-A. and E.V. thank Consorzio per l'Incremento degli Studi e delle Ricerche dei Dipartimenti di Fisica dell'Università degli Studi di Trieste for support. Computational resources have been obtained from CINECA through the ISCRA initiative and the agreement with the University of Trieste. C.A. acknowledges support from MIUR (PRIN 2010-2011 no. 2010N3T9M4).

REFERENCES

- (1) Gokhale, A. A.; Dumesic, J. A.; Mavrikakis, M. *J. Am. Chem. Soc.* **2008**, *130*, 1402–1414.
- (2) Rodriguez, J. a.; Liu, P.; Wang, X.; Wen, W.; Hanson, J.; Hrbek, J.; Pérez, M.; Evans, J. *Catal. Today* **2009**, *143*, 45–50.
- (3) Grabow, L. C.; Mavrikakis, M. *ACS Catal.* **2011**, *1*, 365–384.
- (4) Nerlov, J.; Sckerl, S.; Wambach, J.; Chorkendorff, I. *Appl. Catal. A* **2000**, *191*, 97–109.
- (5) Nerlov, J.; Chorkendorff, I. *Catal. Lett.* **1998**, *54*, 171–176.
- (6) Nerlov, J.; Chorkendorff, I. *J. Catal.* **1999**, *181*, 271–279.
- (7) Monachino, E.; Greiner, M.; Knop-Gericke, A.; Schlögl, R.; Dri, C.; Vesselli, E.; Comelli, G. *J. Phys. Chem. Lett.* **2014**, *5*, 1929–1934.
- (8) Snoeck, J.-W.; Froment, G. F.; Fowles, M. *Ind. Eng. Chem. Res.* **2002**, *41*, 4252–4265.
- (9) Tang, Y.; Liu, J. *Int. J. Hydrogen Energy* **2010**, *35*, 11188–11193.
- (10) Bevilacqua, M.; Filippi, J.; Lavacchi, A.; Marchionni, A.; Miller, H. a.; Oberhauser, W.; Vesselli, E.; Vizza, F. *Energy Technol.* **2014**, *2*, 522–525.
- (11) Weymouth, A. J.; Hofmann, T.; Giessibl, F. J. *Science* **2014**, *343*, 1120–1122.
- (12) Salmeron, M. *Science* **2014**, *343*, 1083–1084.
- (13) Rodriguez, J.; Wayne Goodman, D. *Surf. Sci. Rep.* **1991**, *14*, 1–107.
- (14) Rupprechter, G. *Catal. Today* **2007**, *126*, 3–17.
- (15) Knop-Gericke, A.; Kleimenov, E.; Havecker, M.; Blume, R.; Teschner, D.; Zafeiratos, S.; Schlögl, R.; Bukhtiyarov, V.; Kaichev, V. V.; Prosvirin, I. P.; Nizovskii, A.; Bluhm, H.; Barinov, A.; Dudin, P.; Kiskinova, M. X-Ray Photoelectron Spectroscopy for Investigation of Heterogeneous Catalytic Processes. In *Advances in Catalysis*; Elsevier, 2009; Chapter 4, Vol. 52, pp 213–272.
- (16) Tao, F.; Tang, D.; Salmeron, M.; Somorjai, G. A. *Rev. Sci. Instrum.* **2008**, *79*, 084101.
- (17) Salmeron, M.; Schlogl, R. *Surf. Sci. Rep.* **2008**, *63*, 169–199.
- (18) Kelber, J. *Surf. Sci. Rep.* **2007**, *62*, 271–303.
- (19) Nilus, N. *Surf. Sci. Rep.* **2009**, *64*, 595–659.
- (20) Binns, C. *Surf. Sci. Rep.* **2001**, *44*, 1–49.
- (21) Henry, C. R. *Surf. Sci. Rep.* **1998**, *31*, 231–325.
- (22) Stroppa, A.; Mittendorfer, F. *J. Phys. Chem. C* **2011**, *115*, 21320–21323.
- (23) Engbæk, J.; Lytken, O.; Nielsen, J. H.; Chorkendorff, I. *Surf. Sci.* **2008**, *602*, 733–743.
- (24) Lanzani, G.; Nasibulin, A. G.; Laasonen, K.; Kauppinen, E. I. *Nano Res.* **2009**, *2*, 660–670.
- (25) Jedidi, A.; Norelus, W.; Markovits, A.; Minot, C.; Illas, F.; Abderrabba, M. *Theor. Chem. Acc.* **2013**, *133*, 1430.
- (26) Lang, S. M.; Bernhardt, T. M.; Krstić, M.; Bonačić-Koutecký, V. *Angew. Chem., Int. Ed.* **2014**, *53*, 5467–5471.
- (27) Chiang, H.; Jiang, J. *J. Phys. Chem. C* **2013**, *117*, 12045–12053.
- (28) Wang, F.; Zhang, S.; Li, C.; Liu, J.; He, S.; Zhao, Y.; Yan, H.; Wei, M.; Evans, D. G.; Duan, X. *RSC Adv.* **2014**, *4*, 10834–10840.
- (29) Loveless, B. T.; Buda, C.; Neurock, M.; Iglesia, E. *J. Am. Chem. Soc.* **2013**, *135*, 6107–6121.
- (30) Tao, F.; Dag, S.; Wang, L.-W.; Liu, Z.; Butcher, D. R.; Bluhm, H.; Salmeron, M.; Somorjai, G. *Science* **2010**, *327*, 850–853.
- (31) McCue, A. J.; McRitchie, C. J.; Shepherd, A. M.; Anderson, J. a. *J. Catal.* **2014**, *319*, 127–135.
- (32) Schmid, M.; Kresse, G.; Buchsbaum, A.; Napetschnig, E.; Gritschneider, S.; Reichling, M.; Varga, P. *Phys. Rev. Lett.* **2007**, *99*, 196104.
- (33) Kresse, G.; Schmid, M.; Napetschnig, E.; Shishkin, M.; Köhler, L.; Varga, P. *Science* **2005**, *308*, 1440–1442.
- (34) Ceballos, G.; Song, Z.; Pascual, J. I.; Rust, H.-P.; Conrad, H.; Bäumer, M.; Freund, H.-J. *Chem. Phys. Lett.* **2002**, *359*, 41–47.
- (35) Vesselli, E.; Baraldi, A.; Lizzit, S.; Comelli, G. *Phys. Rev. Lett.* **2010**, *105*, 046102.
- (36) Gritschneider, S.; Degen, S.; Becker, C.; Wandelt, K.; Reichling, M. *Phys. Rev. B: Condens. Matter Mater. Phys.* **2007**, *76*, 014123.
- (37) Degen, S.; Krupski, a.; Kralj, M.; Langner, a.; Becker, C.; Sokolowski, M.; Wandelt, K. *Surf. Sci.* **2005**, *576*, L57–L64.
- (38) Hamm, G.; Barth, C.; Becker, C.; Wandelt, K.; Henry, C. *Phys. Rev. Lett.* **2006**, *97*, 126106.
- (39) Jurczyszyn, L.; Rosenhahn, A.; Schneider, J.; Becker, C.; Wandelt, K. *Phys. Rev. B: Condens. Matter Mater. Phys.* **2003**, *68*, 115425.

- (40) Becker, C.; Rosenhahn, A.; Wiltner, A.; Bergmann, K.; von Schneider, J.; Pervan, P.; Milun, M.; Kralj, M.; Wandelt, K. *New J. Phys.* **2002**, *4*, 75.
- (41) Rosenhahn, A.; Schneider, J.; Becker, C.; Wandelt, K. *Appl. Surf. Sci.* **1999**, *142*, 169–173.
- (42) Wiltner, A.; Rosenhahn, A.; Schneider, J.; Becker, C.; Pervan, P.; Milun, M.; Kralj, M.; Wandelt, K. *Thin Solid Films* **2001**, *400*, 71–75.
- (43) Lehnert, a.; Krupski, a.; Degen, S.; Franke, K.; Decker, R.; Rusponi, S.; Kralj, M.; Becker, C.; Brune, H.; Wandelt, K. *Surf. Sci.* **2006**, *600*, 1804–1808.
- (44) Moors, M.; Krupski, a.; Degen, S.; Kralj, M.; Becker, C.; Wandelt, K. *Appl. Surf. Sci.* **2008**, *254*, 4251–4257.
- (45) Khosravian, H.; Lei, Y.; Uhl, A.; Trenary, M.; Meyer, R. J. *Chem. Phys. Lett.* **2013**, *555*, 7–11.
- (46) Marsault, M.; Wörz, G. H. a.; Sitja, G.; Barth, C.; Henry, C. R. *Faraday Discuss.* **2008**, *138*, 407–420.
- (47) Buchsbaum, A.; De Santis, M.; Tolentino, H. C. N.; Schmid, M.; Varga, P. *Phys. Rev. B: Condens. Matter Mater. Phys.* **2010**, *81*, 115420.
- (48) Baraldi, G.; Comelli, G.; Lizzit, S.; Kiskinova, M.; Paolucci, A. *Surf. Sci. Rep.* **2003**, *49*, 169–224.
- (49) Shirley, D. *Phys. Rev. B* **1972**, *5*, 4709–4714.
- (50) Vêgh, J. J. *Electron Spectrosc. Relat. Phenom.* **2006**, *151*, 159–164.
- (51) Doniach, S.; Sunjic, M. *J. Phys. C: Solid State Phys.* **1970**, *3*, 285–291.
- (52) Giannozzi, P.; Baroni, S.; Bonini, N.; Calandra, M.; Car, R.; Cavazzoni, C.; Ceresoli, D.; Chiarotti, G. L.; Cococcioni, M.; Dabo, L.; Dal Corso, A.; de Gironcoli, S.; Fabris, S.; Fratesi, G.; Gebauer, R.; Gerstmann, U.; Gougoussis, C.; Kokalj, A.; Lazzeri, M.; Martin-Samos, L.; Marzari, N.; Mauri, F.; Mazzarello, R.; Paolini, S.; Pasquarello, A.; Paulatto, L.; Sbraccia, C.; Scandolo, S.; Sclauzero, G.; Seitsonen, A. P.; Smogunov, A.; Umari, P.; Wentzcovitch, R. M. *J. Phys.: Condens. Matter* **2009**, *21*, 395502.
- (53) Vanderbilt, D. *Phys. Rev. B: Condens. Matter Mater. Phys.* **1990**, *41*, 7892–7895.
- (54) Perdew, J. P.; Burke, K.; Ernzerhof, M. *Phys. Rev. Lett.* **1996**, *77*, 3865–3868.
- (55) Olmos-Asar, J. A.; Vesselli, E.; Baldereschi, A.; Peressi, M. *Phys. Chem. Chem. Phys.* **2014**, *16*, 23134–23142.
- (56) Vesselli, E.; Bianchettin, L.; Baraldi, A.; Sala, A.; Comelli, G.; Lizzit, S.; Petaccia, L.; de Gironcoli, S. *J. Phys.: Condens. Matter* **2008**, *20*, 195223.
- (57) Vesselli, E.; Monachino, E.; Rizzi, M.; Furlan, S.; Duan, X.; Dri, C.; Peronio, A.; Africh, C.; Lacovig, P.; Baldereschi, A.; Comelli, G.; Peressi, M. *ACS Catal.* **2013**, *3*, 1555–1559.
- (58) Mårtensson, N.; Nilsson, A. *J. Electron Spectrosc. Relat. Phenom.* **1990**, *52*, 1–46.
- (59) Nilsson, A.; Mårtensson, N. *Phys. Rev. B: Condens. Matter Mater. Phys.* **1989**, *40*, 10249–10261.
- (60) Wurth, W.; Coulman, D.; Puschmann, A.; Menzel, D.; Umbach, E. *Phys. Rev. B: Condens. Matter Mater. Phys.* **1990**, *41*, 12933–12936.
- (61) Gokhale, A. A.; Huber, G. W.; Dumesic, J. A.; Mavrikakis, M. *J. Phys. Chem. B* **2004**, *108*, 14062–14073.
- (62) Van Daelen, M. A.; Li, Y. S.; Newsam, J. M.; van Santen, R. A. *J. Phys. Chem.* **1996**, *100*, 2279–2289.
- (63) Kneitz, S.; Gemeinhardt, J.; Steinrück, H.-P. *Surf. Sci.* **1999**, *440*, 307–320.
- (64) Politano, A.; Formoso, V.; Chiarello, G. *J. Chem. Phys.* **2008**, *129*, 164703.
- (65) An, W.; Liu, P. *J. Phys. Chem. C* **2013**, *117*, 16144–16149.
- (66) Ye, J.; Liu, C. J.; Mei, D.; Ge, Q. *J. Catal.* **2014**, *317*, 44–53.
- (67) Kim, H. Y.; Liu, P. *ChemCatChem* **2013**, *5*, 3673–3679.